Wide range dielectric and infrared spectroscopy of (Nb+In) co-doped rutile ceramics

V. Bovtun,[1] J. Petzelt,[1] M. Kempa,[1] D. Nuzhnyy,[1] M. Savinov,[1] S. Kamba,[1] S. M. M. Yee,[2] and D. A. Crandles[2,*]

[1]*Institute of Physics of the Czech Academy of Sciences, Na Slovance 2, 182 21 Praha 8, Czech Republic*

[2]*Department of Physics, Brock University, St. Catharines, Ontario, Canada L2S 3A1*

(Received 5 January 2018; published 31 July 2018)

The dielectric response of ceramics of co-doped rutile $Ti_{1-x}(Nb_{0.5}In_{0.5})_xO_2$ has been measured via a combination of impedance, high-frequency coaxial, terahertz transmission, and infrared reflectivity spectroscopies spanning 15 decades of frequency between 0.1 Hz and 240 THz. It is argued that the colossal dielectric permittivity reported by Hu *et al.* [Hu *et al.*, Nat. Mater. **12**, 821 (2013)] has the same explanation as in the original colossal permittivity material $CaCu_3TiO_4O_{12}$ (CCTO), namely, a combination of the internal barrier layer capacitor (IBLC) and the surface barrier layer capacitor (SBLC) effects. The IBLC effect is caused by a microstructure consisting of insulating grain boundaries (thickness ~1 nm and conductivity of $\sim 10^{-6}$ S/cm) surrounding interior regions of bulk conductivity approximately equal to 10^{-1} S/cm. The SBLC effect is the result of a depletion layer adjacent to the contacts approximately 100 nm thick with conductivity of 5×10^{-7} S/cm. The SBLC and IBLC effects give rise to dielectric relaxations in low-frequency and radiofrequency regions, respectively. The temperature dependence of both relaxation rates measured down to 20 K is thermally activated. No separate absorption process has been observed that could be linked to giant defect dipoles. Infrared spectroscopy has revealed four weak defect-related modes at frequencies close to the Raman mode frequencies of rutile, activated in the infrared through a symmetry-breaking process. Co-doping produces a significant loss in the partial spectral weight between 75 and 350 cm^{-1} associated with the lowest transverse optical mode, which softens on cooling. The loss in its spectral weight corresponds to the gain in near-infrared spectral weight, previously assigned to small polaron absorption.

DOI: 10.1103/PhysRevMaterials.2.075002

I. INTRODUCTION

Co-doping (doping with equal amounts of donors and acceptors) has been proposed as a method to produce materials with both giant permittivity and low dielectric loss. In the first test, Hu *et al.* [1] processed $Ti_{1-x}(Nb_{0.5}In_{0.5})_xO_2$ ceramics (referred to in this paper as z-NITO where $z = 100x$) and performed impedance spectroscopy. These revealed nearly frequency-independent colossal permittivity (CP) with $\varepsilon' > 10^4$ and low loss ($\tan\delta < 0.1$) for frequencies less than 1 MHz and temperatures 80–400 K [1]. As Nb doping on its own would produce mobile electrons, the authors suggested that the addition of an equal amount of In dopants (co-doping) creates defect clusters which trap the electrons. The authors hypothesized that this process results in giant defect dipoles which causes the combination of high permittivity and low loss. However, no estimate of the dynamics of these localized dipoles was given. Other groups have confirmed the CP response in similar ceramics, mostly with somewhat higher loss values [2–8].

In our recent paper [9], we also have confirmed the CP response of 5-NITO and 10-NITO up to 1 MHz at room temperature. However, this permittivity gradually decreased on cooling to 20 K. In contrast, the dielectric response measured using time-domain terahertz (THz) spectroscopy turned out to be considerably lower and almost independent of temperature and doping level. The difference between the permittivity values for the two frequency ranges indicates that the main dielectric dispersion at room temperature would have to be in the MHz-GHz range and be thermally activated. Moreover, our low-frequency ac conductivity was two orders of magnitude lower than our four-probe dc conductivity and dependent on sample thickness and electrode type. This allowed us to assign the main dielectric dispersion to interface depletion layers between the sample and electrode, i.e., the surface barrier layer capacitor (SBLC) effect. Similar conclusions were reached independently by Song *et al.* [6] who compared the CP behavior of 10-NITO ceramics and single crystals. Single crystals differ in two ways from ceramics: below 1 MHz, the permittivity is lower and there is only one dispersion step, rather than two. The lower-frequency dispersion, observed in both crystals and ceramics, is due to the SBLC effect. The higher-frequency dispersion, observed only in ceramics, is interpreted as the effect of insulating grain boundaries, i.e., the internal barrier layer capacitor (IBLC) effect, which frequently occurs in semiconducting ceramics [10]. A similar explanation was suggested independently by Li *et al.* [3,4], who compared conventionally sintered 1-NITO ceramics with spark plasma sintered ones, with much smaller grains and higher permittivity below 1 MHz. Wu *et al.* [2] also studied the response of 1-NITO ceramics, at room temperature (RT) only up to 110 MHz, where part of the high-frequency dispersion was seen to be strongly dependent on additional sample annealing. Adopting a model of leaky capacitors representing near-electrode layers, grain boundaries and grain bulk, they could estimate the RT values of the three *RC* terms connected in series. Interestingly, the dielectric response of ceramics as well as single crystals is highly nonlinear: with increasing ac voltage, the conductivity increases and permittivity decreases [4,6], as expected for the IBLC and SBLC effects.

*dcrandles@brocku.ca

In this paper, we present our exploration of the dielectric response of 5-NITO and 10-NITO ceramics over 15 decades of frequency—including the GHz, THz, and infrared (IR) range—to determine quantitatively the effect of grain boundaries in addition to near-electrode layers and to observe the possible dispersion of any defect dipoles and the effect of the co-doping process on the IR vibrations. Our results show no dispersion due to any giant dipoles in the grain bulk of our NITO ceramics. It will be shown that both the IBLC and SBLC effects both account for and contribute roughly equally to the CP response.

II. EXPERIMENTAL DETAILS

Samples were made using standard solid-state reactions and sintered for 12 hours at 1400 °C as described in our previous work [9]. The same ceramic pellets—of undoped TiO_2, 5-NITO and 10-NITO—were cut into differently shaped pieces and polished for the various spectroscopic measurements.

First, for the lowest-frequency range ($0.1 \leqslant f \leqslant 10^6$ Hz), we performed impedance spectroscopy (IS) with evaporated gold electrodes on the original pellet (diameter ~10 mm, thickness 1.5 mm) using an Alpha AN (Novocontrol) dielectric analyzer. This pellet was then cut into two semicircular pieces, with one half subsequently shaped into a cylinder of 1 mm diameter and 5 mm length for coaxial reflection measurements on the next higher-frequency (HF) range (1.0 MHz to 1.8 GHz). The cylinders with evaporated gold electrodes on the bases were placed into a Novocontrol BDS2100 sample holder connected to an air coaxial line. The sample holder and coaxial line were enclosed in a SIGMA Systems M18 temperature control chamber (80–450 K). The real and imaginary parts of the dielectric function were extracted by measuring the impedance of the sample and holder combination via an Agilent 4291B RF Impedance/Material Analyzer on cooling with a rate of 1 K/min. The dielectric parameters of the measured ceramics were calculated accounting for the electric-field distribution in the samples [11]. The remaining semicircular piece from the original sample was thinned down to a plate approximately 200 μm thick for THz transmission measurements. The real and imaginary parts of the dielectric function in this spectral region were obtained using a time-domain THz spectrometer based on a Ti:sapphire femtosecond laser with interdigitated photoconducting GaAs photoswitch for generation of the THz pulses and a plate of [110]-oriented ZnTe crystal for detection [12]. For the low-temperature THz measurements, an Oxford Instruments Optistat continuous-He-flow cryostat with Mylar windows was used. IR reflectivity measurements were made using a Bruker IFS 66/V interferometer coupled to a home-built reflectometer built around a continuous-flow Janis helium cryostat. The *in situ* gold evaporation technique [13] was employed to obtain the absolute reflectivity. Different samples, but of the same composition, had to be used for the IR measurements since the first samples were inadequate after forming them for lower-frequency measurements.

Table I lists the sintering temperatures and densities of samples used in this paper. The densities were measured in two different ways: from pellet mass and cylindrical sample dimensions, labeled geometric density ρ_g in the table, and by Archimedes' method, labeled ρ_a, using toluene as the displaced liquid. The measured densities are significantly lower than the theoretical density of rutile (4.23 g/cm^3), consistent with the scanning electron microscope observations of closed and open pores in freshly broken surfaces of the ceramics [9].

TABLE I. Properties of the samples used in this dielectric study of NITO ceramics. Sintering temperatures and measured "geometric" ($\rho_g \pm 0.08$ g/cm^3) and "Archimedes" ($\rho_a \pm 0.01$ g/cm^3) densities are listed in the table. The theoretical density of rutile is 4.23 g/cm^3.

Sample	IS, HF, THz	IR
TiO_2	1400 °C $\rho_g = 3.77$ g/cm^3 $\rho_a = 3.83$ g/cm^3	1300 °C $\rho_g = 3.67$ g/cm^3 $\rho_a = 3.88$ g/cm^3
5-NITO	1400 °C $\rho_g = 3.88$ g/cm^3 $\rho_a = 3.96$ g/cm^3	1450 °C $\rho_g = 3.91$ g/cm^3 $\rho_a = 3.98$ g/cm^3
10-NITO	1500 °C	1450 °C $\rho_g = 3.69$ g/cm^3 $\rho_a = 3.88$ g/cm^3

III. DIELECTRIC FUNCTIONS FOR FREQUENCIES BELOW THE THz RANGE

In Fig. 1, we compare the broadband permittivity (ε'), loss $\tan\delta = \varepsilon''/\varepsilon'$ and ac conductivity $\sigma' = 2\pi f \varepsilon_v \varepsilon''$ (ε_v is the

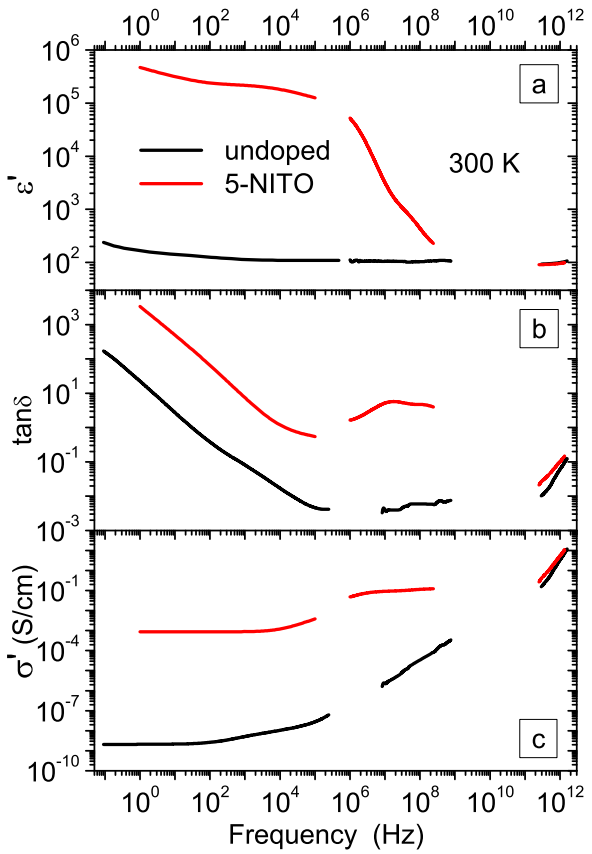

FIG. 1. Broadband spectra of the undoped and 5-NITO ceramics at 300 K: (a) dielectric permittivity, (b) loss tangent, (c) ac conductivity.

vacuum permittivity) spectra of the undoped rutile ceramics with the 5-NITO ceramics at RT. The gaps in the data arise because each measurement technique is valid over a restricted frequency range. The gaps are different for the two samples because the range of validity depends on the value of the real and imaginary parts of the dielectric function in that range. The 10-NITO sample showed a very similar response to that of the 5-NITO sample, and therefore we have omitted its further fitting and quantitative analysis. Note that the low-frequency ac conductivity plateau of the undoped sample ($\sim 10^{-9}$ S/cm) is much higher than the dc conductivity observed in single crystals specially prepared to avoid oxygen loss (where $\sigma_{DC} \approx 10^{-13}$ S/cm) [14]. Thus our undoped sample is likely oxygen deficient, which provides some electrons into the Ti 3*d* orbitals. The HF value of ε' can be accounted for by the tail of the IR vibrations measured with the THz technique. The HF ac conductivity shows the Jonscher universal conductivity response due to hopping carriers [15].

Our 5-NITO sample shows CP behavior ($\varepsilon' > 10^5$) with huge dispersion mainly in the 1–100 MHz range, which we will assign to the IBLC effect, as well as the dispersion below ~100 Hz, which will be assigned to the SBLC effect. The ac conductivity (bottom panel of Fig. 1) shows two plateaus. The HF plateau of value $\sim 10^{-1}$ S/cm ($1 < f < 100$ MHz) can be assigned to the bulk grain conductivity, while the low-frequency plateau ($f < 10$ kHz) of $\sim 10^{-3}$ S/cm is less than the bulk conductivity due to the combined IBLC and SBLC effect, as explained in Ref. [9]. As can be seen in Fig. 1, this value is six orders of magnitude higher than the lowest-frequency conductivity of our undoped sample, while the bulk grain conductivity of the 5-NITO sample is eight orders of magnitude higher than the dc conductivity of the undoped sample.

The temperature dependence of the dielectric function of our 5-NITO sample for selected frequencies up to the THz range is plotted in Fig. 2. Note that as expected for thermally activated dispersion, the permittivity systematically increases with increasing temperature (except for the 293 GHz data, which is strongly influenced by the tail of the IR polar phonon oscillators) but decreases with increasing frequency. The ac conductivity also systematically increases with both temperature and frequency. In Fig. 3, we show our broadband frequency spectra for the same 5-NITO sample at selected temperatures (22–300 K). Previous IS analyses [2,4,6,9] have described the effect of grain boundaries and near-electrode depletion layers using simplified equivalent circuits of leaky capacitors in series. This approach assumes that the permittivities and ac conductivities that determine the values of complex capacitances are frequency independent, which is not realistic for a broad frequency range. This is particularly true for the HF part which describes the grain bulk. Moreover, note that our data were obtained from samples of three different geometries, so that the leaky capacitors have no unique sense. Therefore, for our quantitative analysis up to $\sim 10^{10}$ Hz, we have chosen a model of dielectric relaxations usually used for disordered dielectric materials below the polar-phonon range [16].

To fit the complex dielectric function $\varepsilon^*(f)$, we added two Cole-Cole (CC) relaxations, the loss due to frequency-independent conductivity σ_{DC}, and the lossless THz

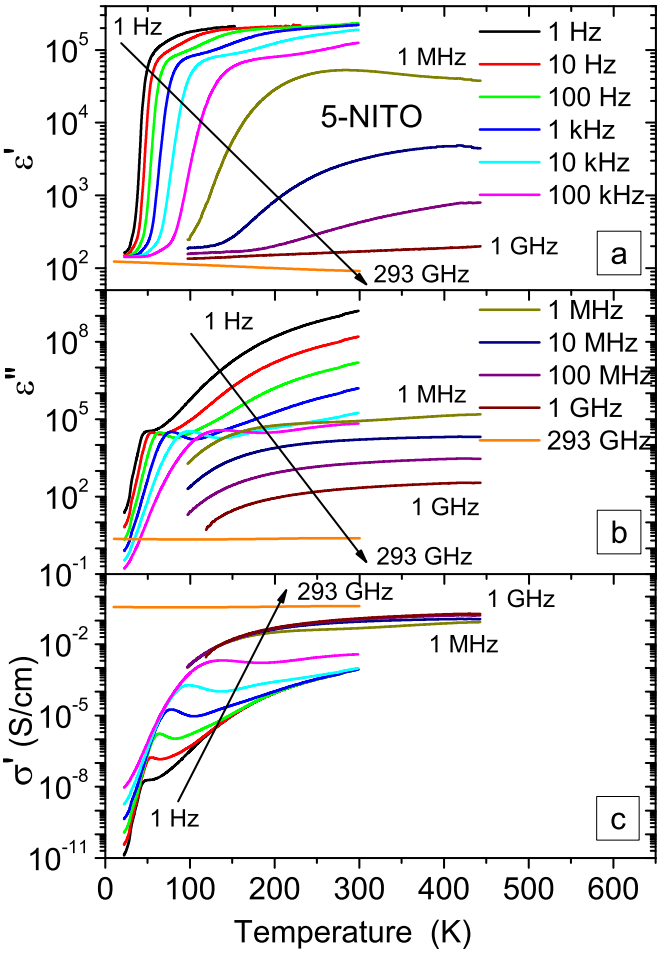

FIG. 2. Temperature dependences of 5-NITO ceramics at selected frequencies: (a) dielectric permittivity, (b) dielectric loss, (c) ac conductivity.

permittivity $\varepsilon_{\mathrm{THz}}$:

$$\varepsilon^*(f) = \varepsilon'(f) - i\varepsilon''(f) = \varepsilon_{\mathrm{THz}} + \frac{\Delta\varepsilon_1}{1 + (if/f_1)^{1-\alpha_1}} + \frac{\Delta\varepsilon_2}{1 + (if/f_2)^{1-\alpha_2}} + \frac{i\sigma_{DC}}{2\pi f \varepsilon_v}. \quad (1)$$

In Eq. (1), f_1 and f_2 are the relaxation rates of fast and slow Cole-Cole relaxations, respectively, with corresponding dielectric strengths $\Delta\varepsilon_1$ and $\Delta\varepsilon_2$ and broadening (diffuseness) parameters α_1 and $\alpha_2 (0 \leqslant \alpha_i \leqslant 1)$. The fits are included in Fig. 3 as solid lines.

The temperature dependences of the fit parameters are plotted in Fig. 4. One can see that the dielectric strengths of both relaxations are almost the same in the whole temperature range and both the relaxation frequencies, which differ by about two orders of magnitude, obey the Arrhenius law. The fast relaxation CC_1 is much less diffusive (with small α_1 close to Debye relaxation) than the slow CC_2. In fact, comparably good fits could be obtained by assuming $\alpha_1 = 0$ in the whole temperature range (i.e., substituting CC_1 by a Debye

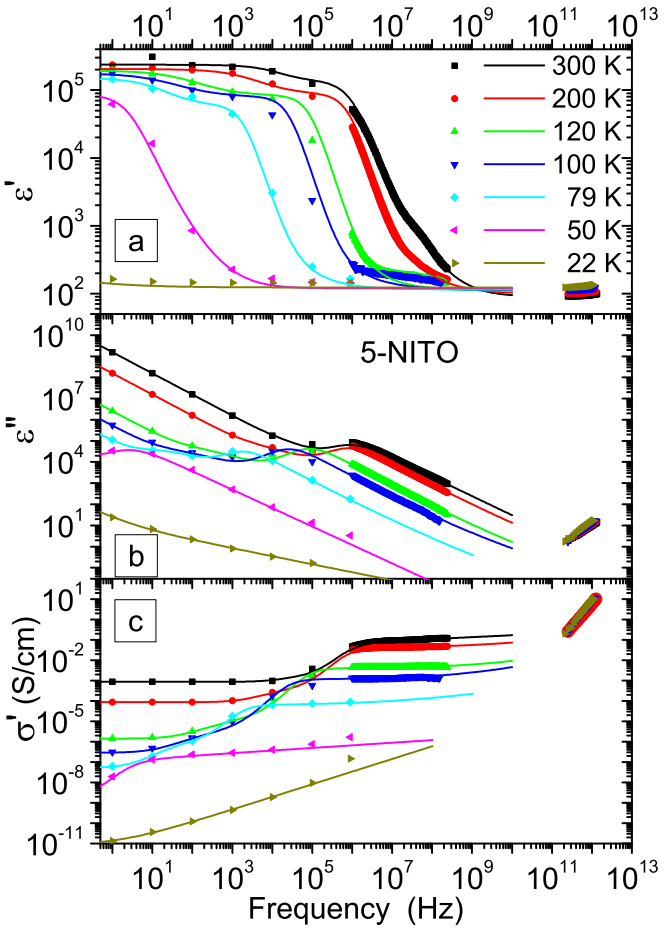

FIG. 3. Broadband spectra of the 5-NITO rutile ceramics at selected temperatures: (a) dielectric permittivity, (b) dielectric loss, (c) ac conductivity. Symbols denote the experimental data; lines correspond to the fits to Eq. (1).

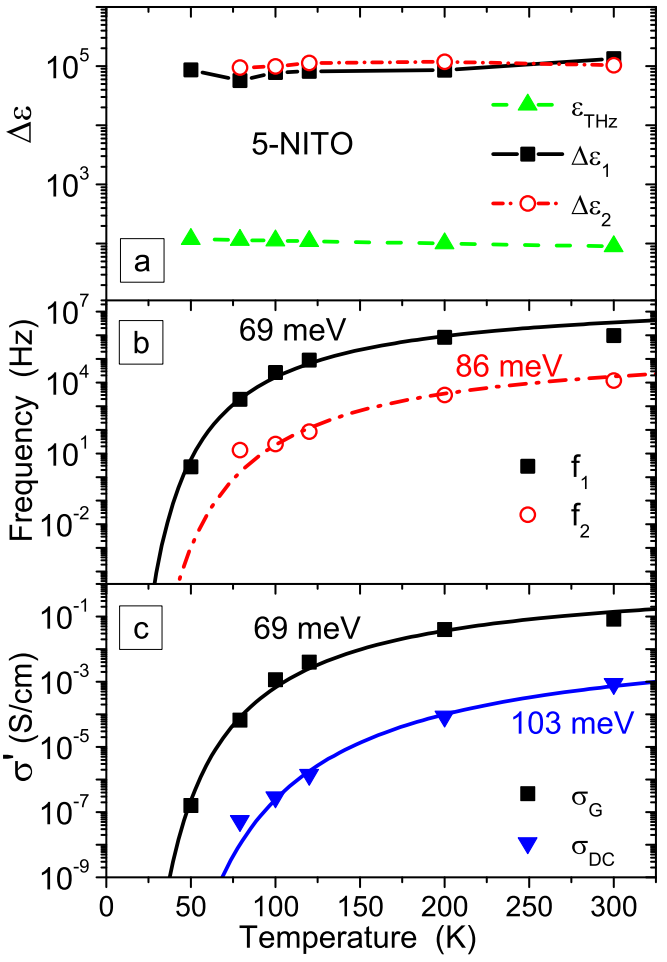

FIG. 4. Parameters of the Cole-Cole fits by Eq. (1) used in Fig. 3 at selected temperatures: (a) dielectric strengths, (b) mean relaxation frequencies, (c) dc and grain-bulk conductivity. The subscripts "1" and "2" denote the parameters ($\Delta\varepsilon$, f) corresponding to the fast CC_1 and slow CC_2 relaxation, respectively. Lines in (b) and (c) correspond to their Arrhenius fits with slightly differing activation energies.

relaxation). The CC_2 relaxation shows increasing diffusivity on cooling (α_2 increases from ~0.25 to ~0.4). From Fig. 3(c), one can see that the ac conductivity, for all temperatures 100–300 K where we have HF data, exhibits a plateau in the HF range fit primarily by the fast relaxation. In our assignment, this represents the grain-bulk conductivity σ_G, whose values (graphically estimated from Fig. 3) are also plotted in Fig. 4(c). Note that σ_G also obeys the Arrhenius law with the same activation energy as f_1, which confirms that this relaxation is the result of less conducting grain boundaries.

To recognize the effect of our CC_1 and CC_2 relaxations on the overall dielectric spectra up to $\sim 10^{10}$ Hz, in Fig. 5 we plot the complex dielectric spectra at 100 K with the contribution of individual terms from Eq. (1). Relaxation frequencies correspond to the maxima in the dielectric loss $\varepsilon''(f)$ spectrum. In Fig. 5(c), we also plotted the Cole-Cole diagram for the overall spectra, showing the effect of individual terms. Note that the solid curve in Fig. 5(c) is a normal Cole-Cole diagram, but the other curves are not. The loss (ε'') for each individual process is plotted against the total permittivity ε' at a given frequency. One can see the effect of the CC_1 which can be attributed to the less conducting grain boundaries. The broad CC_2 can be attributed to the effect of depletion of near-electrode layers at low frequencies, as discussed in Ref. [9], but it contributes to losses up to frequencies much higher than f_2. This feature certainly has no clear physical meaning, but it helps to get a good fit in the GHz range. This is seen even better in Fig. 6, which presents the fitted spectra at 100 K from Fig. 5 recalculated into the real part of ac conductivity and ac resistivity spectra. The complex ac resistivity $\rho^* = 1/\sigma^*$ is used instead of the complex impedance, which has no unique meaning in our case, because the spectra at the low-frequency and HF range are taken from two samples of different geometry. Note again the plateau of the HF bulk-grain conductivity and resistivity in Figs. 6(a) and 6(b), respectively. On the other hand, the CC_2 relaxation provides no conductivity plateau above f_2 due to its diffuseness.

To summarize, the CP effect in our 5-NITO sample can be explained by two contributions of comparable dielectric strengths. The first (CC_1) is due to semiconducting grains, whose bulk conductivity is revealed from the MHz-GHz data with less conducting grain boundaries. The second (CC_2) is

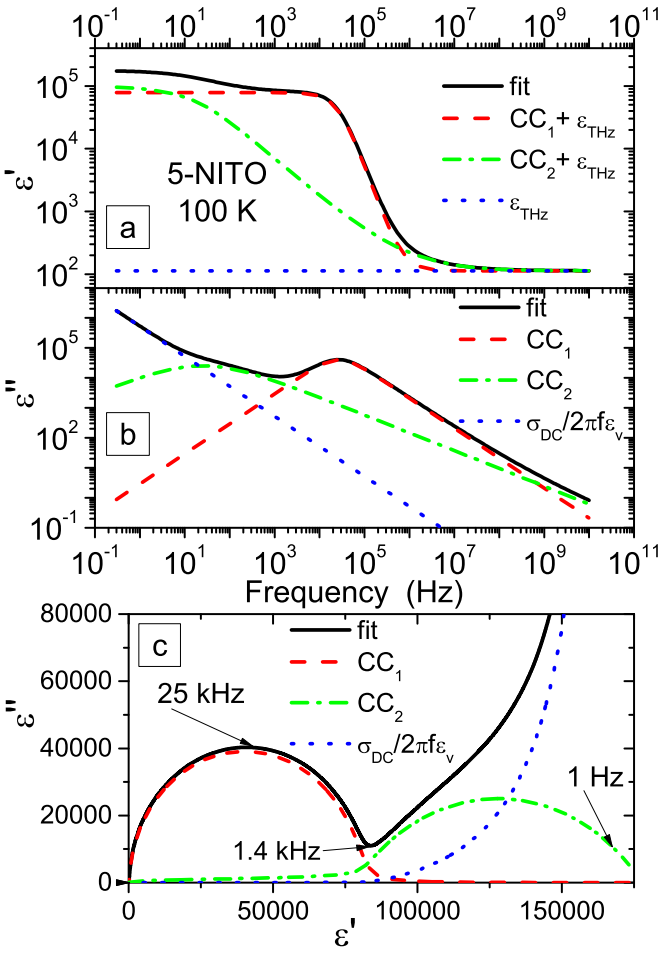

FIG. 5. Contributions to the complex dielectric spectrum of the 5-NITO ceramics at 100 K according to our fit [Fig. 3, Eq. (1)]. Frequency dependences of (a) dielectric permittivity, (b) loss, and (c) Cole-Cole plot, where the solid lines correspond to the fit, dashed and dash-dotted lines correspond to the CC_1 and CC_2 loss contribution, respectively, against the complete permittivity at a given frequency, and dots refer to the corresponding dc conductivity contribution.

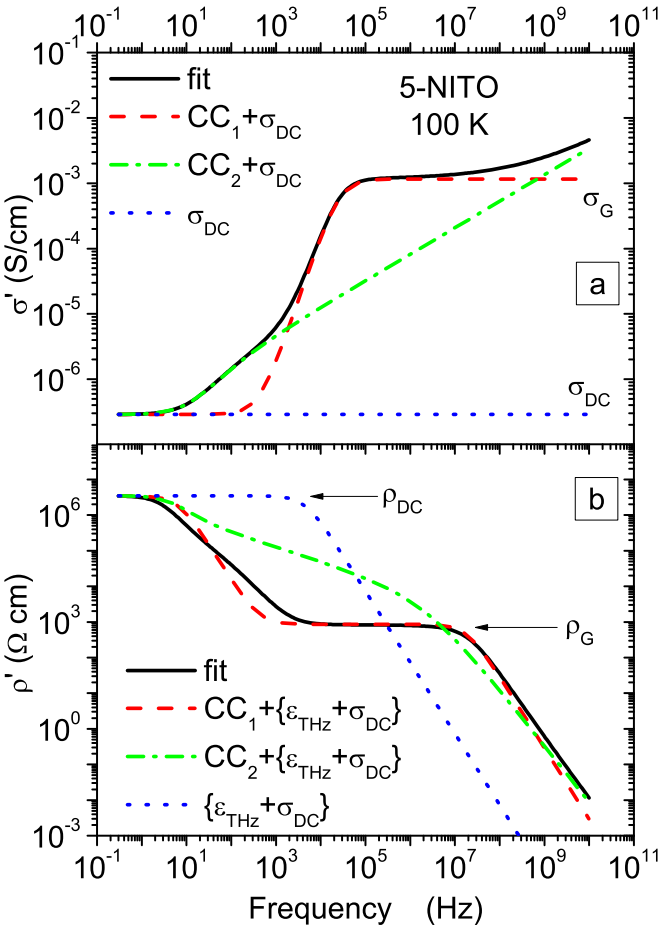

FIG. 6. Contributions to the real parts of (a) ac conductivity and (b) ac resistivity spectra of the 5-NITO ceramics at 100 K calculated from our fit [Fig. 3, Eq. (1)]. Solid lines correspond to the fit, dashed lines to CC_1, dash-dotted lines to CC_2, and dots to the THz permittivity and dc conductivity contributions. The fit of the real part of the ac resistivity in (b) is calculated as $\rho' = \sigma'/[\sigma'^2 + (2\pi f \varepsilon_v \varepsilon')^2]$ and the partial contributions to ρ' are obtained by the same formula, omitting, consequently, in Eq. (1), the term corresponding to CC_2 (dashed line), CC_1 (dash-dotted line), and both CC_2 and CC_1 (dotted line).

due to even more insulating depletion near-electrode layers in combination with the dc conductivity σ_{DC}. The effect of the latter layers was eliminated in our four-point dc conductivity measurements, where the room-temperature dc conductivity of 5-NITO was measured to be 2.2×10^{-2} S/cm (see Fig. 8 and Table I in Ref. [9]). This conductivity represents the response averaged over grain bulk and boundaries. Our data for the grain bulk yields a slightly higher value of 8.3×10^{-2} S/cm. By estimating the average grain size of $\sim10\,\mu$m (see Ref. [9]) and the typical grain boundary thickness of ∼nm (Ref. [3]), the grain boundary conductivity can be estimated to be of the order of 10^{-6} S/cm. This is comparable to the depletion layer conductivity of 5×10^{-7} S/cm (thickness ∼100 nm), evaluated from the model in Ref. [9].

It is remarkable how similar the broadband response functions of 5-NITO and the original CP material $CaCu_3Ti_4O_{12}$ (CCTO) are [17–19]. Three features of the data are almost identical. First, at 300 K, ε' is colossal and almost constant up to the MHz range, where it falls precipitously to a value ∼100 which stays constant up to the THz range. Second, the frequency of the main ε' dispersion decreases with decreasing temperature. At the lowest temperature, ε' is approximately dispersionless and approximately equal to the THz value. Third, the low-frequency conductivity σ' shows a plateau of dc conductivity, which is lower by two orders of magnitude than the value in the HF plateau range, which corresponds to the bulk-grain conductivity. Both conductivities are thermally activated.

CCTO has been intensely studied since the turn of the millennium. Early on in the worldwide study of the material, exotic mechanisms for the CP were proposed but, eventually, on the basis of equivalent circuits of leaky capacitors in series, it was concluded that observations of CP were produced by the IBLC and/or the SBLC effect, exactly the same mechanisms as proposed here (as well as in Refs. [2–4,6]). The basic prerequisite to reach CP appears to be sizeable grain-bulk conductivity (of the order of 10^{-2} S/cm in NITO as well as

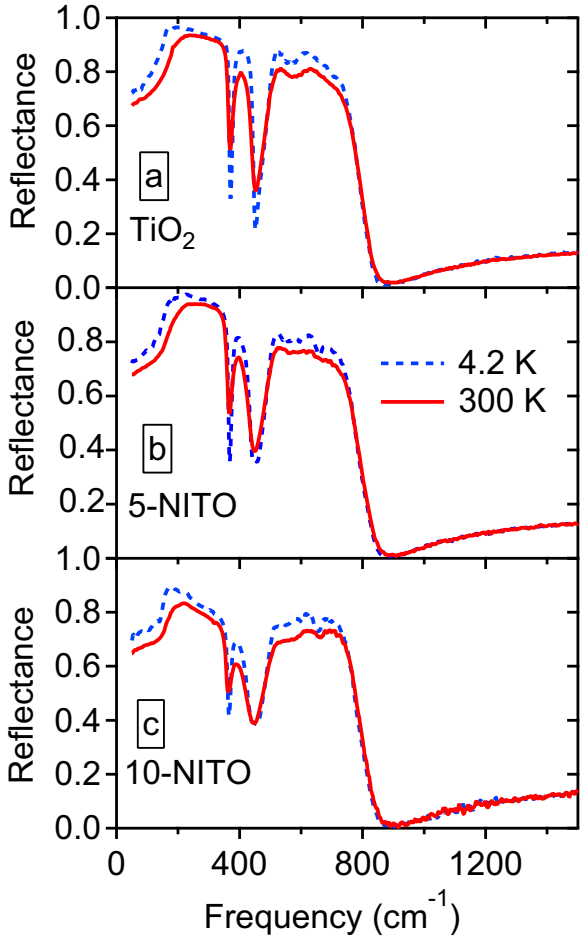

FIG. 7. IR reflectance vs frequency of (a) undoped, (b) 5-NITO, and (c) 10-NITO ceramics.

CCTO), combined with less conducting grain boundaries and depletion layers. It is interesting to note that when a doping process for CCTO was found (Mn substitution for Cu) that reduced the room-temperature conductivity by six orders of magnitude [20], no CP behavior was observed at all.

All the features of the dielectric spectra of Fig. 3 have been accounted for without the need for an absorption process specifically associated with the defect dipoles proposed in Ref. [1]. There is a three-decade gap in frequency in the spectra shown in Fig. 3 between the end of the HF data (≈0.3 GHz) and the beginning of the THz data. Any defect dipole absorption would have to fit in this gap, but could only be extremely weak since at 0.3 GHz the CP dispersion is finished and the permittivity value is equal or only slightly higher than that in the THz range. In the next section, the IR dielectric response, which is the origin of the $\varepsilon_{\mathrm{THz}}$ parameter in our fitting model [Eq. (1)], will be discussed.

IV. INFRARED SPECTROSCOPY

The present reflectance measurements were performed on polycrystalline ceramic samples using unpolarized light. In Fig. 7, note that there are three main high-reflectance bands in both co-doped samples and in undoped rutile. Group theory predicts four IR-active modes ($3E_u + 1A_{2u}$) for the tetragonal rutile structure. Previous IR reflectivity measurements made on single crystals exhibited three high reflectance bands ($3E_u$ modes) and one high reflectance band (A_{2u}) for incident light polarized perpendicular and parallel to the tetragonal c axis, respectively [21]. The reflectance spectrum of the undoped rutile sample shown in Fig. 7(a) looks very much like the single-crystal spectrum with incident light polarized perpendicular to the c axis (E_u modes). Only three bands are observed because the A_{2u} mode and the lowest E_u mode are quite close in frequency and oscillator strength (see Table II). Note the small dip that occurs in the middle (586 cm^{-1}) of the highest-frequency reflectance band of Fig. 7(a). This dip was also observed in the single-crystal measurements at about the same frequency with the same strength in both polarizations. Gervais and Piriou [21] argue that a forbidden mode—perhaps a two-phonon or impurity process—causes the small dip. Note that the edge of the lowest-frequency band redshifts as the temperature decreases for all three co-doping levels. This is associated with the softening mode that was observed previously in single-crystal reflectance measurements as well as neutron and inelastic x-ray scattering [21–23]. One sees that the edges of the three main reflectance bands occur at similar frequencies in all three samples. The most pronounced effect of doping is the fine structure of the lowest- and highest-frequency reflectance bands, suggesting some weak impurity-related modes. In the 10-NITO sample, the reflectance of the lowest-frequency band decreases significantly, which is possibly related [24] to the higher porosity of this sample (see Table I). The leading edge appears to have some fine structure below 180 cm^{-1} and there is a more pronounced downward slope between 200 and 300 cm^{-1} than in the undoped and 5-NITO samples. Finally, while not shown, the reflectance between about 1500 and 8000 cm^{-1} is featureless. A broad IR absorption band centered

TABLE II. Factorized dielectric function parameters found by Gervais and Piriou [21] in their single-crystal reflectivity measurements compared with parameters found fitting the reflectance of undoped TiO_2 in Fig. 7 to the factorized dielectric model. All frequencies and dampings are in cm^{-1}.

Parameter	Ref. [21] 300 K $E \parallel a$	Ref. [21] 300 K $E \parallel c$	Ceramic 300 K	Ceramic 4.2 K
ε_∞	6	7.8	6.54 ± 0.03	6.41 ± 0.03
ω_{TO1}	189	172	182.0 ± 0.6	151.5 ± 0.7
γ_{TO1}	27	76	40 ± 1	27 ± 1
ω_{LO1}	831	796	820.2 ± 0.4	811.7 ± 0.5
γ_{LO1}	50	38	58 ± 1	48 ± 1
ω_{TO2}	381.5		378.7 ± 0.3	380.6 ± 0.2
γ_{TO2}	16.5		21.1 ± 0.6	9.3 ± 0.4
ω_{LO2}	367		367.2 ± 0.2	369.0 ± 0.1
γ_{LO2}	10		14.7 ± 0.4	7.5 ± 0.2
ω_{TO3}	508		487.7 ± 0.4	487.6 ± 0.3
γ_{TO3}	24		39.7 ± 0.8	25.2 ± 0.6
ω_{LO3}	443.5		447.4 ± 0.3	449.2 ± 0.2
γ_{LO3}	21.5		30.7 ± 0.6	14.3 ± 0.3
ω_{TO4}	585	592	589 ± 3	587 ± 3
γ_{TO4}	65	38	72 ± 8	45 ± 7
ω_{LO4}	575	589.5	584 ± 4	585 ± 3
γ_{LO4}	65	55	74 ± 8	48 ± 8

at approximately 0.9 eV (~7000 cm^{-1}) has been observed in previous near-IR transmission measurements in oxygen-reduced or Nb-doped TiO_2 [25,26]. It is associated with small polaron absorption and can be observed with transmission spectroscopy, but it is too weak to have any effect on the reflectance spectra.

The reflectance spectra for the undoped rutile sample were fit using the factorized model [21]:

$$\varepsilon^*(\omega) = \varepsilon_\infty \prod_j \frac{\omega_{\mathrm{LO}j}^2 - \omega^2 + i\omega\gamma_{\mathrm{LO}j}}{\omega_{\mathrm{TO}j}^2 - \omega^2 + i\omega\gamma_{\mathrm{TO}j}}. \quad (2)$$

Here, ε_∞ is the high-frequency permittivity resulting from the electronic absorption processes much above the polar phonons, ω is the linear wave number (frequency in cm^{-1}), $\omega_{\mathrm{TO}j}$ and $\gamma_{\mathrm{TO}j}$ are the transverse-optic (TO) frequency and damping parameter of the jth oscillator, respectively, and $\omega_{\mathrm{LO}j}$ and $\gamma_{\mathrm{LO}j}$ are its respective longitudinal-optic (LO) frequency and damping parameter. The dependence of the normal-incidence reflectivity $R(\omega)$ on the dielectric function is given by

$$R(\omega) = \left| \frac{\sqrt{\varepsilon^*(\omega)} - 1}{\sqrt{\varepsilon^*(\omega)} + 1} \right|^2. \quad (3)$$

The factorized model fitting parameters for the undoped sample at 300 and 4.2 K appear in Table II. Note from the table that at 300 K, the lowest TO mode for the polycrystalline undoped sample is between ω_{TO} measured in single crystals along the a and c axes, as expected. Note that the 300 K scattering rates for the ceramics are all larger than the corresponding single-crystal values and that there is a discrepancy of several percent in some of the ω_{TO} and ω_{LO} values. This may be an effect of the porosity and averaging over the grain anisotropy, which will be the topic of an independent paper [27]. As expected, the scattering rates γ_{TO} and γ_{LO} all decrease with decreasing temperature, as shown in Table II.

Because of the complexity of the impurity-induced fine structure observed in Fig. 7, it was decided that Kramers-Kronig (KK) analysis is an easier approach to study the doping dependence of the impurity modes. For the KK phase integral, reflectivity data were generated using the model discussed above for $\omega < 50\,cm^{-1}$. Between 50 and 7000 cm^{-1}, the data measured in this work were used. Between 7000 and 82 000 cm^{-1}, the reflectance data of Cardona and Harbeke [28] were used with appropriate weighting (2/3 a-axis, 1/3 c-axis). Between 140 000 and 2.4×10^8 cm^{-1}, the x-ray reflectance was generated according to the procedure of Ref. [29]. A smooth interpolation was created between the UV reflectance data and the x-ray reflectance. The free-electron approximation was used for frequencies above the x-ray reflectance [30].

Figure 8, which compares the dielectric loss function $[-\mathrm{Im}(1/\varepsilon^*)]$ and σ' calculated via KK analysis for undoped TiO_2 at 300 K allows a check of the factorized model parameters. The peaks in σ' should correspond to ω_{TO}, while the peaks in the loss function should correspond to ω_{LO}. Note the agreement of these frequencies to within less than ≈0.5% with the parameters of Table II, except for the ≈1% difference in ω_{TO3}. The broad peaks associated with the forbidden mode (ω_{TO4} and ω_{LO4}) are barely visible in Fig. 8.

The real optical conductivity at $T = 4.2$ K extracted using the KK transformation of the reflectance data appears in Fig. 9. In the undoped ceramic spectrum, one can observe the three strongest IR-active modes centered at $\omega \approx 155$, 390, and 500 cm^{-1}. The weak forbidden mode is marked ω_{TO4} in Fig. 9 and in Table II. It is a very broad and weak mode which can barely be distinguished from the wings of the IR-active mode near 500 cm^{-1} in the undoped sample spectrum, and not at all in spectra of the 5-NITO and 10-NITO samples. On the other hand, there appear to be four impurity modes that increase in oscillator strength with co-doping level centered near $\omega \approx 136$, 447, 654, and 800 cm^{-1}. It is interesting to note that four Raman-active modes were previously observed [31] in rutile at $\omega \approx 143$, 447, 612, and 826 cm^{-1}. It is possible that the co-doping process causes the Raman modes to develop a dipole moment and become weakly IR active.

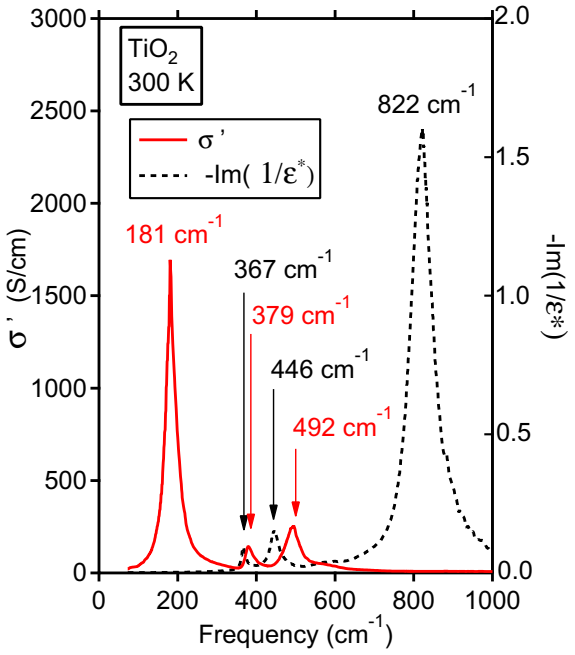

FIG. 8. KK real optical conductivity and dielectric loss function for undoped rutile at 300 K.

Consider one of the curious features of Fig. 9(a), which is the decrease in oscillator strength with co-doping level in the lowest transverse mode. Optical sum rules are a powerful tool to study both free and bound charge carriers [32]. One of these rules states that the spectral weight,

$$W = \int_{\omega_a}^{\omega_b} \sigma'(\omega) d\omega \quad (4)$$

(or oscillator strength), should be conserved as temperature changes if the charge associated with a particular absorption process is constant. For example, when integrated over all frequencies, the spectral weight is proportional to the constant total electron density. Changes over more restricted frequency ranges—a partial spectral weight—yield clues as to changes in bonding environment [33] and/or electronic structure [34]. There are at least two factors that could contribute to the decrease in measured oscillator strength suggested by Fig. 9(a): sample porosity—in which case no conclusions can be reached about bonding environment—and/or transfer of spectral weight. Porosity does affect the measurements, as

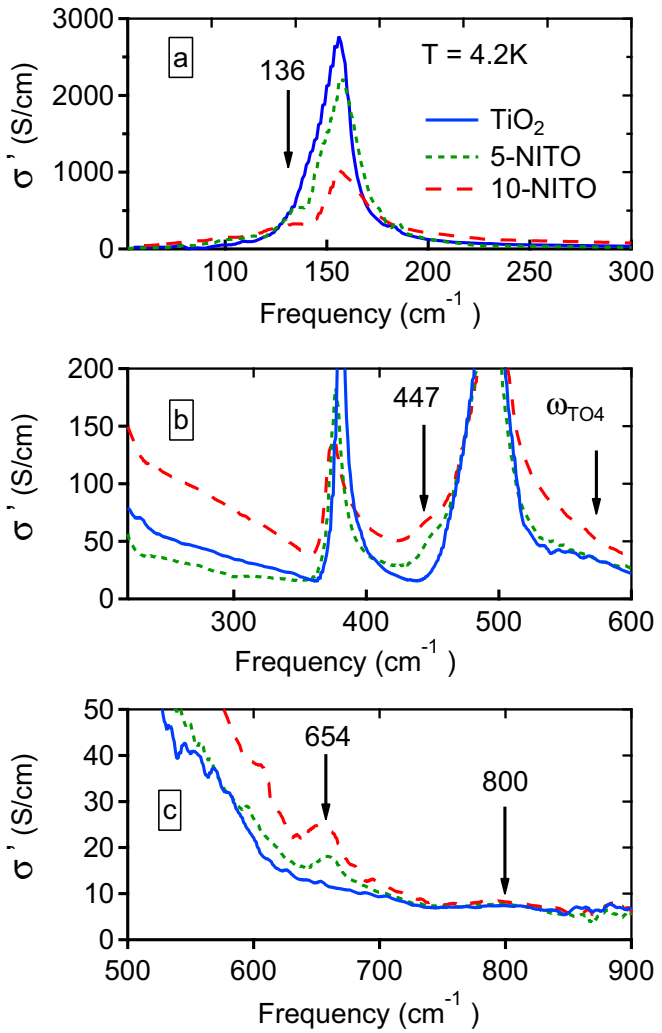

FIG. 9. The real optical conductivity as determined by KK analysis of the reflectivity at 4.2 K for TiO_2, 5-NITO and 10-NITO.

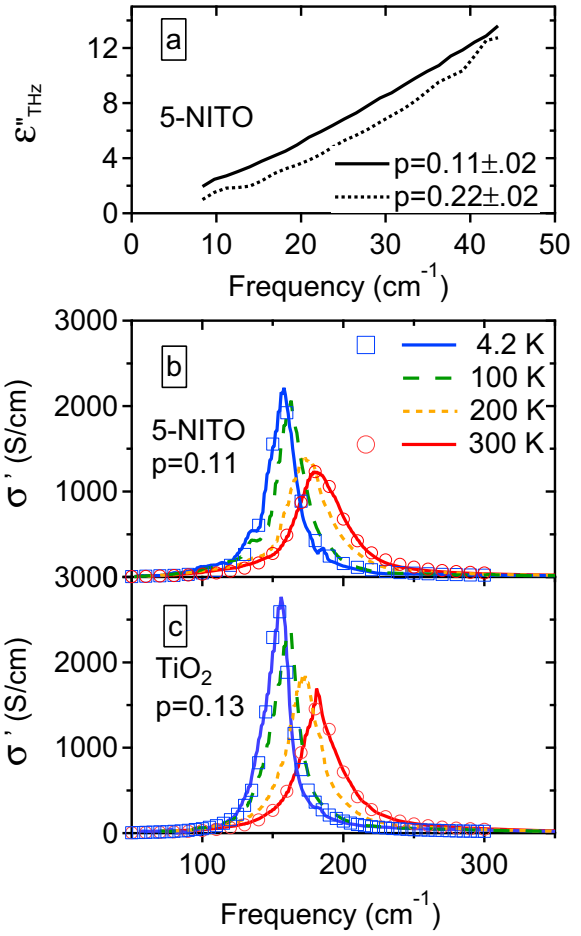

FIG. 10. (a) ε'' vs frequency measured using THz transmission for 5-NITO samples of two different porosities. (b) The KK real conductivity of 5-NITO ceramic as a function of temperature. (c) The KK real conductivity of undoped ceramic as a function of temperature compared with fits to a Lorentz oscillator (open circles, squares).

illustrated in Fig. 10(a) which plots the imaginary part of the dielectric function in the THz region for two samples of 5-NITO of different (geometrical) porosity. Note that the more porous sample exhibits the smaller measured ε'', as expected in an effective medium picture. So it is important to compare samples of roughly the same porosity when commenting on spectral weight. Figures 10(b) and 10(c) compare the temperature and frequency dependence of the KK optical conductivity of 5-NITO and undoped rutile samples of approximately equal porosity. Note that the peak height is about 25% smaller for the co-doped sample which, because these are samples of equal porosity, suggests that doping does induce a loss of spectral weight. The doping dependence of the spectral weight associated with the soft mode was analyzed in two ways.

First, fits were made of the real optical conductivity of the lowest mode—the data of Figs. 10(b) and 10(c). The classical Lorentz oscillator model with three parameters, i.e., resonance frequency ω_o, scattering rate Γ, and strength ω_p, was used:

$$\sigma'(\omega) = \frac{\omega^2\Gamma}{60} \cdot \frac{\omega_p^2}{\left(\omega_o^2 - \omega^2\right)^2 + \omega^2\Gamma^2}. \qquad (5)$$

In Eq. (5), the units of the conductivity are S/cm, while the units of ω_o, Γ, and ω_p are cm^{-1}. Second, the partial spectral weight [Eq. (4)] for the data shown in Figs. 10(b) and 10(c) was calculated between 75 and 350 cm^{-1}. The results of these two analyses are shown in Fig. 11(c).

The temperature dependence of the three Lorentz oscillator parameters is illustrated in Figs. 11(a)–11(c). Note the softening of the mode with decreasing temperature in Fig. 11(a). In Fig. 11(b), it is shown that the scattering rate decreases with temperature as it should and increases with doping (or increased disorder). Figure 11(c) shows that the strength of the mode as measured by the Lorentz oscillator strength $\omega_p(T)$ is approximately temperature independent. Also shown in Fig. 11(c) is the partial spectral weight. Note that the difference between TiO_2 and 5-NITO in spectral weight $\Delta W \approx 5000\,S/cm^2$ (~8%) is approximately temperature independent.

A question arises as to which part of the spectrum the partial spectral weight is transferred since the total spectral weight should be conserved. In an attempt to answer this question, we turn to old studies of the IR transmission of reduced rutile [25,26]. Heating in a reducing atmosphere produces oxygen

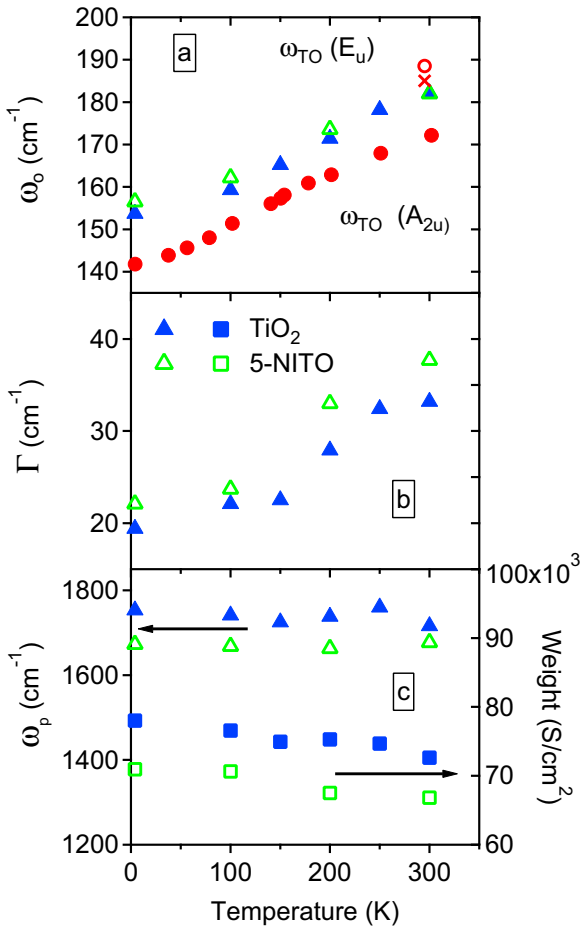

FIG. 11. Lorentz oscillator (a) resonance frequency (ω_o) vs temperature. Also shown are neutron-scattering measurements [22] (filled and empty red circles) and an inelastic x-ray scattering measurement [23] (red X). (b) Scattering rate (Γ) and (c) strength (ω_p) of undoped TiO_2 (filled blue triangles) and 5-NITO (unfilled green triangles). Also shown is the partial spectral weight of the KK conductivity integrated between 75 and 350 cm^{-1} for undoped TiO_2 (filled blue squares) and 5-NITO (open green squares).

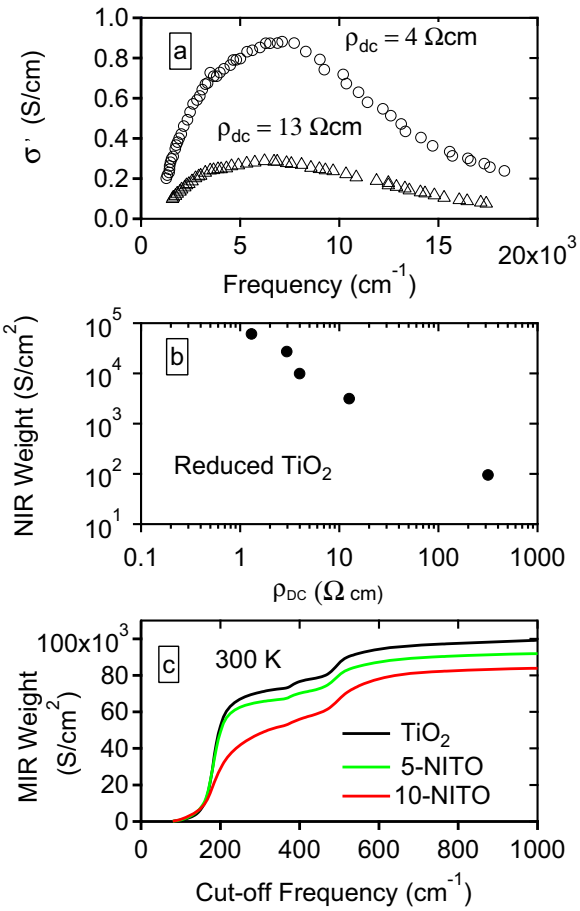

FIG. 12. (a) Real optical conductivity for reduced TiO_2 as a function of dc resistivity. (b) Spectral weight of the near-IR absorption band between 2000 and 20 000 cm^{-1} at room temperature vs room-temperature dc resistivity. (Data in (a) and (b) are from Ref. [26]). (c) Partial spectral weight between 75 cm^{-1} and a cutoff frequency as a function of the cutoff frequency.

vacancies which are believed to create n-type carriers and increase the dc conductivity as well as a NIR absorption, which is observable in transmission measurements. In Fig. 12(a), data are shown for samples of different dc resistivity. Note that the magnitude of the NIR absorption band increases as the dc resistivity decreases. This peak has been attributed to small polaron absorption [25]. The partial spectral weight between 2000 and 20 000 cm^{-1} extracted from Cronemeyer's RT absorption coefficient data [26] is plotted in Fig. 12(b). It is interesting to note that for rutile crystals of dc conductivity ~0.1 S/cm (matching σ_{DC} of our 5-NITO ceramics as reported in Ref. [9]), the spectral weight associated with the NIR absorption band is approximately equal to the partial spectral weight lost in the soft-mode region (~5000 S/cm^2). This strongly suggests that charge associated with the lowest optical mode is also associated with the hopping conductivity process in co-doped rutile, i.e., its eigenvector is coupled with the charges providing the small polaron absorption.

Figure 12(c) shows the partial spectral weight associated with the IR-active modes as a function of the upper cutoff frequency, where the lower cutoff frequency was fixed at 75 cm^{-1}. Note that the two highest curves in Fig. 12(c) are almost parallel for $\omega > 300$ cm^{-1}, above the tail of the lowest mode. Thus the only difference between the spectral weight associated with IR-active modes in undoped and 5-NITO is in the mode that softens. In the 10-NITO sample, it looks like the spectral weight loss occurs over several modes, not just the lowest-frequency one. However, if the upper cutoff frequency is above the highest-frequency optical modes (say 850 cm^{-1}), the partial spectral weight appears constant. Recall that the 10-NITO sample is significantly more porous than the other two samples (see Table I), so it is difficult to draw any conclusions.

V. CONCLUSIONS

A striking resemblance between the dielectric response over 15 orders of magnitude between CCTO and NITO has been observed. Like in CCTO, the colossal dielectric permittivity at RT is the result of a relatively high grain-bulk electrical conductivity (~10^{-1} S/cm) and a combination of the SBLC and IBLC effects. The effects in the whole temperature range of 20–300 K were well described by fitting the dielectric

spectra from 0.1 up to 10^{10} Hz by two thermally activated Cole-Cole relaxations combined with a dc conductivity contribution and a lossless THz permittivity, which describes the TO polar-phonon contribution. The activation energies of the dc and bulk-grain conductivities are ∼100 and ∼70 meV, respectively, as expected for electron-hopping conduction. In combination with Ref. [9], the thickness and conductivity of the depletion near-electrode layer were estimated to 100 nm and 5×10^{-7} S/cm, respectively, and the grain boundaries of ∼nm thicknesses with conductivities of the order of 10^{-6} S/cm.

Four defect modes have been observed in the IR conductivity of NITO samples evaluated by KK at frequencies close to the Raman frequencies of rutile. These may be Raman-active modes that become IR active through a symmetry-breaking process. Co-doping produces a significant loss in the partial spectral weight associated with the lowest-frequency TO mode. The loss in spectral weight is of the same order of magnitude as the gain in NIR spectral weight observed in transmission measurements in samples of comparable dc resistivity and assigned to small polaron absorption.

ACKNOWLEDGMENTS

This research was supported by the National Science and Engineering Research Council of Canada (2017-04785), the Czech Science Foundation (Projects No. 15-08389S and No. 18-09265S) and Operational Programme Research, Development and Education financed by European Structural and Investment Funds and the Czech Ministry of Education, Youth and Sports (Project No. SOLID21-CZ.02.1.01/0.0/0.0/16_019/0000760). D.C. thanks the Dept. of Dielectrics of the Institute of Physics CAS for kind hospitality.

[1] W. B. Hu, Y. Liu, R. L. Withers, T. J. Frankcombe, L. Noren, A. Snashall, M. Kitchin, P. Smith, B. Gong, H. Chen, J. Schiemer, F. Brink, and J. Wong-Leung, Nat. Mater. **12**, 821 (2013).
[2] Y. Q. Wu, X. Zhao, J. L. Zhang, W. B. Su, and J. Liu, Appl. Phys. Lett. **107**, 242904 (2015).
[3] J. Li, F. Li, C. Li, G. Yang, Z. Xu, and S. Zhang, Sci. Rep. **5**, 8295 (2015).
[4] J. Li, F. Li, Y. Zhuang, L. Jin, L. Wang, X. Wei, Z. Xu, and S. Zhang, J. Appl. Phys. **116**, 074105 (2014).
[5] H. Han, P. Dufour, S. Mhin, J. H. Ryu, C. Tenailleau, and S. Guillemet-Fritsch, Phys. Chem. Chem. Phys. **17**, 16864 (2015).
[6] Y. Song, X. Wang, Y. Sui, Z. Liu, Y. Zhang, H. Zhan, B. Song, Z. Liu, Z. Lv, L. Tao, and J. Tang, Sci. Rep. **6**, 21478 (2016).
[7] S. Ke, T. Li, M. Ye, P. Lin, W. Yuan, X. Zeng, L. Chen, and H. Huang, Sci. Rep. **7**, 10144 (2017).
[8] Z. Li, X. Luo, W. Wu, and J. Wu, J. Am. Cer. Soc. **100**, 3004 (2017).
[9] D. A. Crandles, S. M. M. Yee, D. Nuzhnyy, M. Savinov, J. Petzelt, S. Kamba, and J. Prokes, J. Appl. Phys. **119**, 154105 (2016).
[10] M. Li, Z. Shen, M. Nygren, A. Feteira, D. C. Sinclair, and A. R. West, J. Appl. Phys. **106**, 104106 (2009).
[11] J. Grigas, *Microwave Dielectric Spectroscopy of Ferroelectrics and Related Materials* (Gordon and Breach, Australia, 1996).
[12] P. Kuzel, H. Nemec, F. Kadlec, and C. Kadlec, Opt. Express **18**, 15338 (2010).
[13] C. C. Homes, M. Reedyk, D. A. Crandles, and T. Timusk, Appl. Opt. **32**, 2976 (1993).
[14] R. G. Breckenridge and W. R. Hosler, Phys. Rev. **91**, 793 (1953).
[15] A. K. Jonscher, Nature (London) **267**, 673 (1977).
[16] *Broadband Dielectric Spectroscopy*, edited by F. Kremer and A. Schonals (Springer-Verlag, Berlin, 2003).
[17] S. Krohns, P. Lunkenheimer, S. G. Ebbinghaus, and A. Loidl, Appl. Phys. Lett. **91**, 022910 (2007).
[18] Ch. Kant, T. Rudolf, F. Mayr, S. Krohns, P. Lunkenheimer, S. G. Ebbinghaus, and A. Loidl, Phys. Rev. B **77**, 045131 (2008).
[19] P. Lunkenheimer, S. Krohns, S. Riegg, S. G. Ebbinghaus, A. Reller, and A. Loidl, Eur. Phys. J. Spec. Top. **180**, 61 (2010).
[20] M. Li, A. Feteira, D. C. Sinclair, and A. R. West, Appl. Phys. Lett. **88**, 232903 (2006).
[21] F. Gervais and B. Piriou, Phys. Rev. B **10**, 1642 (1974).
[22] J. G. Traylor, H. G. Smith, R. M. Nicklow, and M. K. Wilkinson, Phys. Rev. B **3**, 3457 (1971).
[23] B. Wehinger, A. Bosak, and P. T. Jochym, Phys. Rev. B **93**, 014303 (2016).
[24] D. Nuzhnyy, J. Petzelt, I. Rychetsky, and G. Trefalt, Phys. Rev. B **89**, 214307 (2014).
[25] V. N. Bogomolov, E. K Kudinov, D. N. Mirlin, and Yu. A. Firsov, Fiz. Tver. Tela **9**, 2077 (1967) [Sov. Phys. Solid State **9**, 1630 (1968)].
[26] D. C. Cronemeyer, Phys. Rev. **113**, 1222 (1959).
[27] T. Ostapchuk *et al.* (unpublished)
[28] M. Cardona and G. Harbeke, Phys. Rev. **137**, A1467 (1965).
[29] D. B. Tanner, Phys. Rev. B **91**, 035123 (2015).
[30] F. Wooten, *Optical Properties of Solids* (Academic Press, New York, 1972).
[31] S. P. S. Porto, P. A. Fleury, and T. C. Damen, Phys. Rev. **154**, 522 (1967).
[32] D. Y. Smith, *Handbook of Optical Constants of Solids* (Academic Press, New York, 1985).
[33] C. C. Homes, T. Vogt, S. M. Shapiro, S. Wakimoto, M. A. Subramanian, and A. P. Ramirez, Phys. Rev. B **67**, 092106 (2003).
[34] M. M. Qazilbash, A. A. Schafgans, K. S. Burch, S. J. Yun, B. G. Chae, B. J. Kim, H. T. Kim, and D. N. Basov, Phys. Rev. B **77**, 115121 (2008).